Precise Fermi level engineering in a topological Weyl semimetal via fast ion implantation

Manasi Mandal,[1, 2, †] Abhijatmedhi Chotrattanapituk,[1, 3, †] Kevin Woller,[2] Lijun Wu,[4] Haowei Xu,[2] Nguyen Tuan Hung,[1, 5] Nannan Mao,[3] Ryotaro Okabe,[1, 6] Artittaya Boonkird,[1, 2] Thanh Nguyen,[1, 2] Nathan C. Drucker,[1, 7] Xiaoqian M. Chen,[8] Takashi Momiki,[9] Ju Li,[2, 10] Jing Kong,[3] Yimei Zhu,[4] and Mingda Li[1, 2, *]

[1]*Quantum Measurement Group, MIT, Cambridge, MA 02139, USA*
[2]*Department of Nuclear Science and Engineering, MIT, Cambridge, MA 02139, USA*
[3]*Department of Electrical Engineering and Computer Science, MIT, Cambridge, MA 02139, USA*
[4]*Condensed Matter Physics and Materials Science Department,*
Brookhaven National Laboratory, Upton, NY 11973-5000, USA
[5]*Frontier Research Institute for Interdisciplinary Sciences (FRIS), Tohoku University, Japan*
[6]*Department of Chemistry, MIT, Cambridge, MA 02139, USA*
[7]*School of Engineering and Applied Sciences, Harvard University, Cambridge, MA 02138, USA*
[8]*Brookhaven National Laboratory, Upton, NY 11973-5000, USA*
[9]*Aisin Technical Center of America, Inc, CA 95110, USA*
[10]*Department of Materials Science and Engineering, MIT, Cambridge, MA 02139, USA*
(Dated: May 6, 2024)

The precise controllability of the Fermi level is a critical aspect of quantum materials. For topological Weyl semimetals, there is a pressing need to fine-tune the Fermi level to the Weyl nodes and unlock exotic electronic and optoelectronic effects associated with the divergent Berry curvature. However, in contrast to 2D materials, where the Fermi level can be controlled through various techniques, the situation for bulk crystals beyond laborious chemical doping poses significant challenges. Here, we report the meV-level ultra-fine-tuning of the Fermi level of bulk topological Weyl semimetal TaP using accelerator-based high-energy hydrogen implantation and theory-driven planning. By calculating the desired carrier density and controlling the accelerator profiles, the Fermi level can be experimentally fine-tuned from 5 meV below, to 3.8 meV below, to 3.2 meV above the Weyl nodes. High-resolution transmission electron microscopy reveals the crystalline structure is largely maintained under irradiation, while electrical transport indicates that Weyl nodes are preserved and carrier mobility is also largely retained. Our work demonstrates the viability of this generic approach to tune the Fermi level in semimetal systems and could serve to achieve property fine-tuning for other bulk quantum materials with ultrahigh precision.

The precise controllability of the Fermi level and carrier doping in a solid-state material holds paramount significance in condensed matter physics and materials science. In microelectronics such as high-electron-mobility transistors, the ability to fine-tune the Fermi level is crucial to control the operation thresholds and high-frequency responses [1–3]. In strongly correlated systems such as high-temperature cuprate superconductors, achieving optimal hole doping is essential for enhancing the superconducting critical temperature [4–6]. As for energy harvesting applications such as thermoelectrics, a well-adjusted Fermi level strikes a delicate balance between electrical conductivity and thermopower, which leads to an optimized power factor [7–10]. A particularly noteworthy utilization for Fermi level fine-tuning lies in topological materials, where only a precisely positioned Fermi level can unveil the topological properties. For instance, in topological insulators, dissipationless electronic states such as quantum anomalous Hall states can only manifest when the Fermi level is located precisely within the small surface bandgap. This can only be achieved through a strategic blend of chemical doping [11–13] and electrostatic gating in thin heterostructures [14–17]. For topological Weyl semimetals (WSM), exotic phenomena like large charge-to-spin interconversion [18, 19], strong higher-order photoresponse [20, 21],

anomalous Nernst effect [22, 23], and quantized thermoelectric Hall effect [24, 25] emerge due to a divergent Berry curvature, which can only happen when the Fermi level is tuned to be exactly at the Weyl nodes.

However, unlike in lower dimensional materials, where the Fermi level can be continuously fine-tuned through a variety of accessible techniques like electrostatic and ionic gating, achieving this level of control in three-dimensional bulk materials has presented a longstanding challenge. Chemical doping can only be performed during the synthesis and offers limited precision, which does not meet the stringent requirement for topological semimetals. The electronic states in topological semimetals, such as from the Weyl and Dirac bands, have a linear dispersion with zero density-of-states at the topological singularities, making the Fermi level location extremely sensitive to the carrier concentration [26, 27]. Therefore, there is an urgent need to attain enhanced fine-tunability of topological semimetals for more practical energy and information applications.

In this work, we use high-energy, accelerator-based hydrogen implantation to achieve ultra-fine carrier doping in WSM of tantalum phosphide (TaP) [24]. Although hydrogenation and low-energy ion implantation have been used to tune materials properties [28–33], there are a few key distinct features presented in the current setup. Foremost, the fine controllability of the advanced accelerator technique enables an ultra-fine tuning of the Fermi level down to the meV regime, far beyond the previous approaches. In addition, the high energy beam

---

† These authors contribute to this work equally.
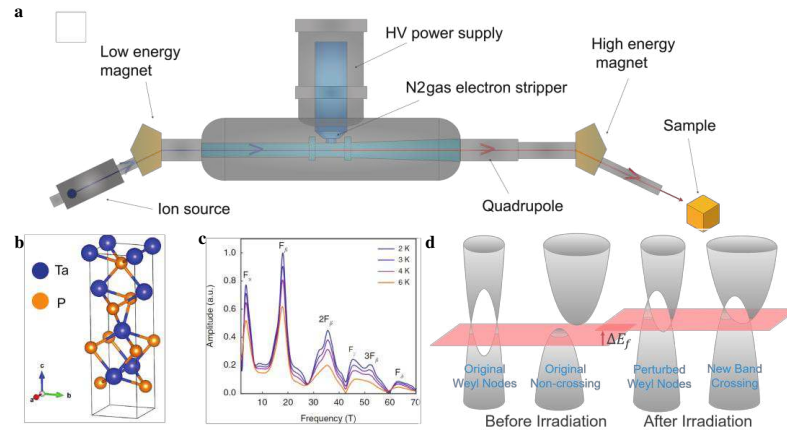* manasim@mit.edu; zhu@bnl.gov; mingda@mit.edu

FIG. 1. **a)** Tandem accelerator schematic. It includes an ion source to produce negative ions. Selected ion species are injected toward the terminal using a low-energy magnet. The ion beam is focused by a magnetic quadrupole lens, and the desired ion species are directed into the beamline for the experiment. **b)** Crystal structure of the Weyl semimetal TaP. **c)** Fast Fourier transform of the longitudinal magnetoresistance of TaP reveals quantum oscillations with specific frequencies (reproduced from [24]). **d)** Illustration of the irradiation effect on the TaP's band structure (gray scale surface), and Fermi level (red plane). The red arrow indicates the shift of Fermi level (ΔE_f). The diagrams also show the perturbation in Weyl nodes' positions (third diagram from left) from the original (left most), as well as, new Weyl nodes introduced from band crossing (right most compares to second from left) when the structure got H doped.

also enables the doping of a bulk crystal beyond a thin film with tens of nanometers thickness [30, 31, 34]. Moreover, thanks to the rapid development of the accelerator technology with high precision control of the accelerator beam energy and flux of ions, we were able to achieve *a priori* doping planning through a combination of DFT and Monte Carlo calculations, which eventually shows quantitative agreement with actual experiments. This sets up an example for ultrafine doping planning experiments. High-resolution transmission electron microscopy (HRTEM), particularly scanning transmission electron microscopy with high-angle annular dark-field (STEM-HAADF) imaging, shows the presentation of high-quality crystal preservation under irradiation with stacking faults within the depth about 200 nm. It is well known that in high T_c superconductors, heavy-ion irradiation typically leads to stacking faults near amorphized ion tracks [35, 36]. However, in our case with hydrogen implantation, the low stopping power preserves the structural integrity of TaP without generating visible amorphous tracks, voids, or defects. Despite the observation of stacking faults within a 200nm depth from the sample surface, likely induced by the kinetic energy of H-ion bombardment causing rigid lattice shifts, electric transport, and carrier mobility remain intact. On the other hand, the temperature to reach the charge neutral point is nearly doubled. Notably, inversion symmetry is not restored, which is crucial for Weyl node formation, potentially explaining the preservation of Weyl nodes under irradiation (Fig. 5).

The doping experiment uses the Tandem accelerator located at the Center for Science and Technology with Accelerators

and Radiation (CSTAR). The schematic used in our experiment is shown in Fig. 1a. This type of accelerator consists of two successive linear accelerators with the same power supply. A cesium sputtering source is used as the ion source to generate negative ions from most of the elements with low vapor pressure (excluding noble gases). This source works by cesium sputtering a solid target, which produces negative ions that are then subjected to electron exchange with neutral cesium. Negative ions are initially introduced into the first stage (blue arrow), where they are accelerated toward the positive high-voltage (HV) terminal. Subsequently, depending on the experimental preferences, nitrogen gas can be injected into the HV terminal to strip some of the electrons from the ions, which transforms them into positive ions. As a result, the Tandem accelerator enables a remarkable capability to dope tens of different elements in the period table of elements. We have chosen negative hydrogen as the dopant, which offers several advantages in materials science due to its small atomic size, i.e., it does not significantly alter the structure of pristine materials [37]. Electrochemical hydrogenation can also be used for electron doping of semiconductors with good doping regime controllability but not high-precision doping level control [38]. In addition, hydrogen can exhibit a range of exotic properties as a dopant that makes it particularly interesting for research and applications, including metal-to-insulator transitions [39], magnetostriction [40], enhanced superconductivity [41], and paraelectric-to-ferroelectric phase transitions [42].

The earlier study [24] highlights TaP as a remarkable topological Weyl semimetal with an inversion symmetry-breaking
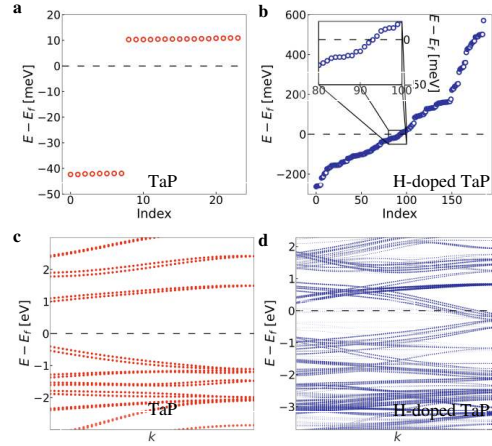
FIG. 2. Ab initio calculation of Weyl nodes' energy relative to Fermi level (E_f) of **a)** pristine TaP, and **b)** H-doped TaP, $Ta_{16}P_{16}$ supercell with one H insertion (detail in Sec. SI-4 of Supplementary Information (SI)). Each plot point represents a Weyl node placed in its energy ascending order from left to right, starting with index 0. The inset in **b** shows the zoom-in view of the Weyl nodes with energy near Fermi level. **d)** Unfolded band structure of H-doped TaP that pass through a Weyl node in **b**. **c)** Unfolded band structure of pristine TaP along the same path as **d**. The y-axes' zero points are not aligned to compensate Fermi level shift.

crystal structure (Fig. 1b). It exhibits a non-saturating thermopower, a giant magnetoresistance, and a quantized thermoelectric Hall effect. Shubnikov-de Haas oscillations (SdH) are observed in the background-subtracted MR (ΔMR) data at temperatures below 25 K. The Fourier transform of ΔMR showed four pockets, with two small carrier pockets, one with a low-frequency $F_a = 4$ T and the other with $F_\beta = 18$ T, indicating the presence of two Weyl nodes' levels (W1, and W2) relative to Fermi level (Fig. 1c) [24]. Introducing H^- ions through irradiation is expected to shift the Fermi level, perturb the existing Weyl nodes, and introduce new band crossings, as illustrated in the schematic diagram in Fig. 1d.

To quantitatively link the hydrogen implantation profile to the shift of the Fermi level in TaP, we build a simple model, which shows that the required doping dosage is on the order of 10_{19} cm^{-3} in order to shift the Fermi level to one of the Weyl nodes (details in Sec. SI-1 of Supplementary Information (SI)). We also support this theoretical model with density functional theory (DFT) [43, 44] calculations from Quantum ESPRESSO [45, 46] package, which gives the same order of dosage requirements (details in Sec. SI-2).

To understand the defect structures and characteristics, we employ Quantum ESPRESSO and Vienna *ab initio* simulation package (VASP) [47, 48], which provide quantitative information on H defects' characteristics inside TaP as well as qualitative insight into the energy redistribution of Weyl node

energy levels upon H doping. With standard supercell method, we specify the most probable interstitial sites for H defects to be at (0, 0, 1/6) distance from every Ta conventional unit cell (also shown in Fig. S7a in SI). Our calculation also determines the zero-point formation Gibbs free energy of an interstitial H defect in TaP to be 0.226 eV. After that, a nudge elastic band (NEB) [49] method is performed to determine both H defects' migration path ways, and their respective migration barrier. The calculations show lowest migration barrier of 1.45 eV, and the anisotropy of defect diffusion which favor the (0, 0, 1) direction by six folds (details in Sec. SI-3).

We also perform band structure calculation of H-doped TaP, providing direct computational evidence on the preservation of Weyl nodes upon doping. The energy of the Weyl nodes with respect to the Fermi level (E_f) is shown in Fig. 2a for TaP and Fig. 2b for the doped TaP system (one H in $Ta_{16}P_{16}$). Here, the horizontal axis is the index of the Weyl nodes. The Weyl nodes are ranked according to their energy, so the index itself does not carry additional reciprocal space information. Notably, the doped TaP system exhibits Weyl nodes that are distributed somewhat continuously. One of the Weyl nodes near Fermi level in Fig. 2b got selected, and unfolded band structure of a short path that pass through the node's position is shown in Fig. 2c (pristine TaP), and Fig. 2d (H-doped TaP). Comparing these results, our DFT calculations indicate that the doping actually shifts the Fermi level, perturbs band structure, and introduce additional band crossings (of which, some can be Weyl nodes) as hypothesized. However, it is important to note that this DFT calculation is for one H in $Ta_{16}P_{16}$ corresponding to $\sim 10_{21}$ cm^{-3} doping concentration which is two orders of magnitude higher than intended. Furthermore, in an actual experiment, it is impossible to periodically dope H at the same interstitial site for every supercell. Because of these, we should expect our experiment to be affected by Fermi level shift, broadening, and appearance of minor peaks not corresponding to the perturbed W1, and W2.

To calculate the implanted ion energy, penetration depth within the crystal, and damage to the target material, the stopping and range of ions in matter software (SRIM/TRIM) [50] was employed. The detailed calculations are presented in Sec. SI-5. Single crystals of TaP were irradiated with 20 keV H$^-$ ions with varying durations to achieve the desired doping concentration. The summary of different samples with their respective dose of irradiation and time duration is presented in Table 1.

To see the effect of ion implantation on the possible change of the crystal structures, particularly excluding the effect from radiation damage, we have performed HRTEM, including STEM-HAADF measurements on the $S3_m$ sample in both non-irradiated regime away from ion implantation direction (Fig. 3) and irradiated regimes (Fig. 4), respectively. As shown from STEM-HAADF images (Fig. 4a), hydrogen implantation only has minimal radiation disturbance to the TaP crystal compared to the pristine regime (Fig. 3a), with moderate stacking fault created at the shallow region up to 200 nm (Fig. 3b). We observed no significant extended defects such as voids or precipitates, nor did we find evidence of radiation-induced segregation or amorphization. Notably, even with the
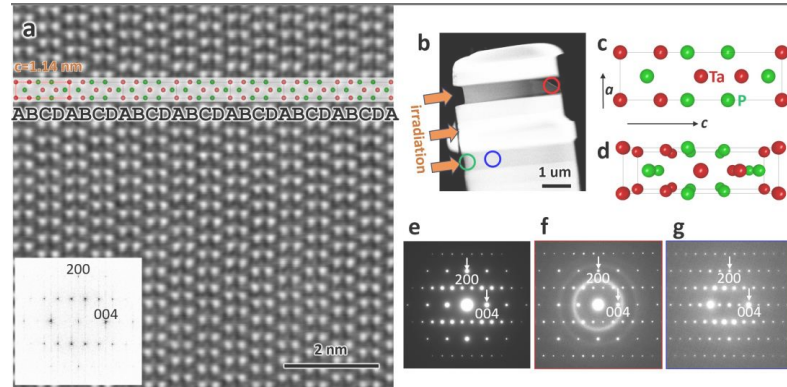
FIG. 3. **a)-b)** STEM-HAADF images viewed along [010] direction. **a** is from a thin defect-free area marked by a red circle in **b**. The stacking is perfect ABCDABCD. . . **c)-d)** Structure model of TaP (I4$_1$md with a = 3.3184 Å and c = 11.363 Å): **c** [010] projection, and **d** 3D prospective view. The [010] projection is embedded in **a**. Because Ta (Z = 73) is much heavier than P (Z = 15), only Ta columns are visible. The inset is the FFT of the image in **a**, which is consistent with kinematic diffraction simulation in **e)**. **f)-g)** Electron diffraction patterns (EDP) from the area marked by red (thin area) and blue (thick area) circles in **b**, respectively. We note the reflection spots in FFT and EDPs are sharp and forbidden reflections appear in **g** due to multiple scattering.
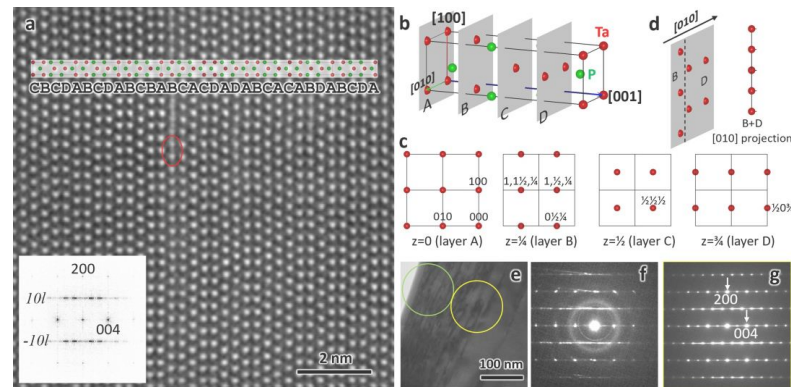

FIG. 4. **a)** [010] STEM-HAADF image from area marked by the green circle in Fig. 3(b), revealing stacking faults that deviate from the ABCDABCD... order shown in the embedded structure model of the pristine crystal. The left-bottom inset is the FFT of the image. The spots in *10l* and *-10l* elongated along *c** axis, confirms the stacking faults along *c* axis. In the area marked by red ellipse, B and D layers overlapped along the beam direction [010] (see **d** for details). **b)** TaP structure model. **c)** Ta layer at z = 0, 0.25, 0.5 and 0.75, respectively. The TaP crystal can be considered as stacking of the four layers (A, B, C, and D) along the *c* direction. The relative atomic arrangement in these four layers is identical if the rigid lattice shift is ignored. The shift of B, C and D layer respect to the A layer is $0\ \frac{1}{2}\frac{1}{4}$, $0\ \frac{1}{2}\frac{1}{2}$ and $^1 0\frac{3}{2}$, respectively, in the pristine crystal. The radiation track of H implantation may induce the layer in-plane shift (*a/b* direction), resulting in stacking faults. **d)** 3D view (left) and [010] projection (right) of the layer consisting of B and D layers. **e)-g)** HRTEM image (**e**) and EDPs from the area marked by (f) green and (g) yellow circles. The diffraction spots elongate along *c** direction due to stacking faults.

formation of stacking faults, inversion symmetry is not being restored (Fig. 4). Since the inversion symmetry breaking is the prerequisite for the formation of Weyl nodes, the lack of inversion in the stacking fault regime may explain why Weyl nodes are largely preserved under irradiation (shown in Fig. 5). More HRTEM images are shown in Sec. SI-7. The preservation of crystallinity is further supported by synchrotron X-ray diffraction with very minor peak broadening (Sec. SI-6).
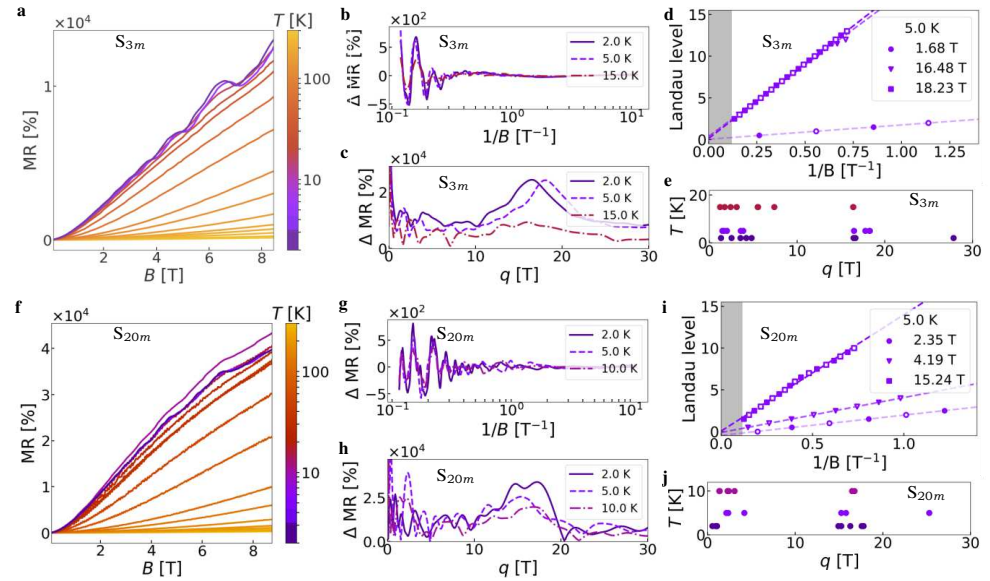
FIG. 5. **a)** Variation of magnetoresistance (MR) with magnetic field (B) at different temperatures for sample S_{3m}. **b)** Background-subtracted MR (ΔMR) of **a** versus 1/B for a few temperatures that exhibit Shubnikov-de Haas (SdH) oscillations. This ΔMR is calculated using q polynomial-fitted background subtraction. **c)** Fast Fourier transform (FFT) of **b**. **d)** Example of a Landau level fan diagram analysis which indicates the presence of lower frequencies in **b** at 5 K than TaP [24]. The greyed out area indicate the region corresponding to magnetic field larger than 9 T, i.e., larger than the measurement range. **e)** Scatter plot of the oscillation frequencies extracted from Background-subtracted MR using various background subtraction methods at low temperatures. **f)-j)** are the same as **a)-e)**, but for the S_{20m} sample.

The irradiated samples S_{3m} and S_{20m} exhibit a significantly high magnetoresistance (MR) on the order of $10^4\%$ and accompanied by SdH oscillations at temperatures below 15 K (see Fig. 5a, and Fig. 5f, respectively). In contrast, the S_{2h} sample does not display such oscillations even up to 9 T (details in Sec. SI-9). It is important to note that the analysis of carrier pockets based on quantum oscillations can be influenced by the choice of the background for MR. Therefore, we calculated the background-subtracted MR (ΔMR) using different background subtraction methods (details in Sec. SI-9).

Sample	Dose of irradiation (cm^{-2})	Irradiation time (minutes)	Doping Concentration (cm^{-3})
S_{3m}	1.25×10^{15}	3	$\sim 10^{19}$
S_{20m}	1.23×10^{16}	20	$\sim 10^{20}$
S_{2h}	1.23×10^{17}	120	$\sim 10^{21}$

TABLE 1. Summary of TaP samples irradiated with H$^-$ ions for different durations.

Fig. 5b, and Fig. 5g illustrate the ΔMR obtained with a polynomial-fitted background subtraction method, while Fig. 5c, and Fig. 5h show the corresponding fast Fourier transform (FFT) results for S_{3m} and S_{20m}, respectively. These FFT plots reveal a noticeably lower oscillation frequency, as well as the appearance of minor peaks compared to the pristine TaP [24]. Furthermore, Fig. 5d, and Fig. 5i present the results of the Landau level (LL) fan diagram analysis, which indicates the presence of more oscillations with lower frequencies. This finding supports and validates our DFT calculations concerning the preservation of Weyl nodes in proximity to the Fermi surface compared to pristine TaP. The oscillation frequencies have been repeatedly extracted using various background subtraction methods, and scatter plotted together to show agreement between methods (see Fig. 5e, and Fig. 5j). Our analysis indicates the shift in relative energy of Fermi level from 5 meV below W1 for pristine TaP, to 3.8 meV below W1 for S_{3m}, and to 3.2 meV above W1 for S_{20m} (details in Sec. SI-1).

To find the effect of irradiation on the carrier concentration and the mobility Fig. 6, the longitudinal and transverse conductivity data were fitted with a two-band model. The details of the data extraction from these measurements are discussed in Sec. SI-8. The compensation temperature increased to 160 K and 155 K for S_{3m} and S_{20m}, respectively, whereas it is 110 K for pristine TaP [24]. Fig. 7 shows the normalized carrier concentration n_T extracted from the simple extended Kohler's
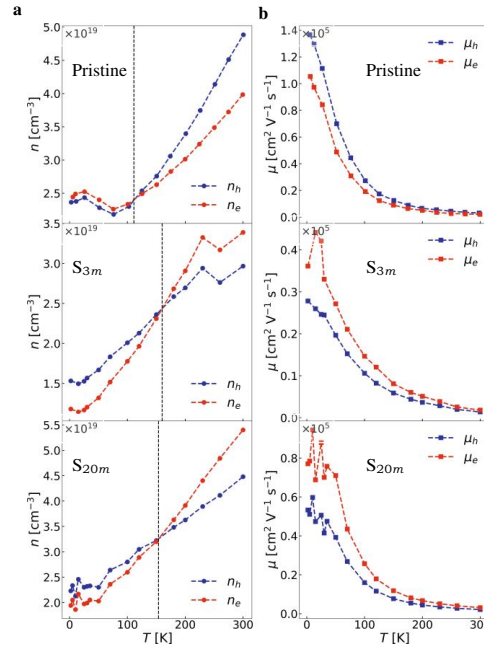
FIG. 6. **a)** Temperature-dependent profiles of electron (n_e) and hole concentrations (n_h). **b)** Temperature-dependent trends of electron (μ_e) and hole mobilities (μ_h). The top profiles serve as references for TaP. Our analysis involves the extraction of equivalent profiles from the two-band model fitting, applied to the S_{3m} and S_{20m} samples as annotated in the plots.

rule. The consistent temperature-dependent trend observed in our analysis, in accordance with the fitted two-band model, serves as compelling evidence for the accuracy and validity of our findings (see Sec. SI-10 for detailed calculation).
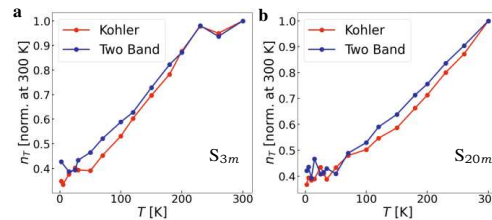

FIG. 7. Direct comparison of the temperature dependence of the normalized adjusted parameter n_T, as extracted from both the extended Kohler's rule and the two-band model for **a)** S_{3m}, and **b)** S_{20m}. The plots show good agreement between simple extended Kohler's rule and fitted two-band model.

In summary, we have addressed a novel method for ultra-fine Fermi level tuning in the prototype bulk WSM TaP using high-energy hydrogen implantation facilitated by accelerator-based techniques. HRTEM and XRD show the high-quality crystals after ion implantation. The transport measurements demonstrate a successful increment in the charge neutral point temperature through precise tuning of the Fermi level in proximity to the Weyl nodes. These experimental results are achievable by the guidance of DFT calculations. The approach presented in this study represents a highly controllable and universally applicable technique for fine-tuning the Fermi level and quantum orderings in bulk quantum materials. By enabling precise control over the Fermi level in bulk crystals, the work could open up new possibilities for exploring and manipulating the unique properties of topological WSM and other quantum materials. This advancement holds significant promise for the development of future quantum technologies and applications.

SUPPLEMENTARY MATERIAL

The Supplementary Material contains the following information: 1. Theoretical modeling of doped TaP, linking radiation profiles to dopant concentration. 2-4. ab initio calculations of H-doped TaP. 5. SRIM/TRIM simulation. 6. X-ray diffraction. 7. Additional TEM images. 8. Carrier concentration and motilities. 9. Quantum oscillation, and 10. Kohler's rule analysis on transport.

ACKNOWLEDGMENTS

[1] V. Hemaja and D. Panda, Silicon **14**, 1873 (2022).

[2] H. Lee, J. Perozek, L. D. Rosario, and C. Bayram, Sci. Rep. **6**, 37588 (2016).

[3] M. A. Khan, A. Bhattarai, J. N. Kuznia, and D. T. Olson, Appl. Phys. Lett. **63**, 1214 (1993).

[4] M. A. Hossain, J. D. Mottershead, D. Fournier, A. Bostwick, J. L. McChesney, E. Rotenberg, R. Liang, W. N. Hardy, G. A. Sawatzky, I. S. Elfimov, D. A. Bonn, and A. Damascelli, Nat. Phys. **4**, 527 (2008).

[5] B. Michon, C. Berthod, C. W. Rischau, A. Ataei, L. Chen, S. Komiya, S. Ono, L. Taillefer, and A. Georges, Nat. Commun. **14**, 3033 (2023).

[6] C. Weber, K. Haule, and G. Kotliar, Nat. Phys. **6**, 574 (2010).

[7] G. Kim, L. Shao, K. Zhang, and K. P. Pipe, Nat. Mater. **12**, 719 (2013).

[8] L. Wu, X. Li, S. Wang, T. Zhang, J. Yang, W. Zhang, L. Chen, and J. Yang, NPG Asia Mater. **9**, e343 (2017).

[9] S. Tsuda, A. Yoshinari, S. Takezawa, K. Ohishi, N. Nagamura, W. Zhang, Y. Iwasaki, and Y. Takagiwa, Mater. Res. Express **10**, 055506 (2023).

[10] Y. Pei, J. He, J. Li, F. Li, Q. Liu, W. Pan, C. Barreteau, D. Berardan, N. Dragoe, and L. Zhao, NPG Asia Mater. **5**, e47 (2013).

[11] C.-Z. Chang, J. Zhang, X. Feng, J. Shen, Z. Zhang, M. Guo, W. Li, Y. Ou, P. Wei, L.-L. Wang, Z.-Q. Ji, Y. Feng, S. Ji, X. Chen, J. Jia, X. Dai, Z. Fang, S.-C. Zhang, K. He, Y. Wang, Y. Lu, X.-C. Ma, and Q.-K. Xue, Science **340**, 167 (2013).

[12] S. Kang, S. Kang, H. Kim, and J. Yu, npj 2D Mater. Appl. **7**, 13 (2023).

[13] X. Zhang, L. Liu, and W. Liu, Sci. Rep. **3**, 2908 (2013).

[14] G. M. Ferguson, R. Xiao, A. R. Richardella, D. Low, N. Samarth, and K. C. Nowack, Nat. Mater. **22**, 1100 (2023).

[15] C. Zhang, T. Zhu, T. Soejima, S. Kahn, K. Watanabe, T. Taniguchi, A. Zettl, F. Wang, M. P. Zaletel, and M. F. Crommie, Nat. Commun. **14**, 3595 (2023).

[16] Y. Deng, Y. Yu, M. Z. Shi, Z. Guo, Z. Xu, J. Wang, X. H. Chen, and Y. Zhang, Science **367**, 895 (2020).

[17] W. Lin, Y. Feng, Y. Wang, J. Zhu, Z. Lian, H. Zhang, H. Li, Y. Wu, C. Liu, Y. Wang, J. Zhang, Y. Wang, C.-Z. Chen, X. Zhou, and J. Shen, Nat. Commun. **13**, 7714 (2022).

[18] B. Zhao, D. Khokhriakov, Y. Zhang, H. Fu, B. Karpiak, A. M. Hoque, X. Xu, Y. Jiang, B. Yan, and S. P. Dash, Phys. Rev. Research **2**, 013286 (2020).

[19] J. B. S. Mendes, A. S. Vieira, R. O. Cunha, S. O. Ferreira, R. D. Dos Reis, M. Schmidt, M. Nicklas, S. M. Rezende, and A. Azevedo, Adv. Mater. Interfaces **9**, 2201716 (2022).

[20] G. B. Osterhoudt, L. K. Diebel, M. J. Gray, X. Yang, J. Stanco, X. Huang, B. Shen, N. Ni, P. J. W. Moll, Y. Ran, and K. S. Burch, Nat. Mater. **18**, 471 (2019).

[21] J. Ma, Q. Gu, Y. Liu, J. Lai, P. Yu, X. Zhuo, Z. Liu, J.-H. Chen, J. Feng, and D. Sun, Nat. Mater. **18**, 476 (2019).

[22] P. Li, J. Koo, W. Ning, J. Li, L. Miao, L. Min, Y. Zhu, Y. Wang, N. Alem, C. Liu, Z. Mao, and B. Yan, Nat. Commun. **11**, 3476 (2020).

[23] S. Roychowdhury, M. Yao, K. Samanta, S. Bae, D. Chen, S. Ju, A. Raghavan, N. Kumar, P. Constantinou, S. N. Guin, N. C. Plumb, M. Romanelli, H. Borrmann, M. G. Vergniory, V. N. Strocov, V. Madhavan, C. Shekhar, and C. Felser, Adv. Sci. **10**, 2207121 (2023).

[24] F. Han, N. Andrejevic, T. Nguyen, V. Kozii, Q. Nguyen, T. Hogan, D. Z., P. S., S. B., A. A., A. E., C. S., H. S., F. L., and L. M., Nat. Commun. **11**, 6167 (2020).

[25] E. F. Scott, K. A. Schlaak, P. Chakraborty, C. Fu, S. N. Guin, S. Khodabakhsh, A. E. Paz y Puente, C. Felser, B. Skinner, and S. J. Watzman, Phys. Rev. B **107**, 115108 (2023).

[26] H. Iohani, P. Foulquier, P. Le Fèvre, F. m. c. Bertran, D. Colson, A. Forget, and V. Brouet, Phys. Rev. B **107**, 245119 (2023).

[27] J. Liu, L. X. Linchao Ding, X. Li, K. Behnia, and Z. Zhu, J. Phys. Condens. Matter **35**, 375501 (2023).

[28] L. Xie, Q. Zhu, G. Zhang, K. Ye, C. Zou, O. V. Prezhdo, Z. Wang, Y. Luo, and J. Jiang, J. Am. Chem. Soc. **142**, 4136 (2020).

[29] S. Kang, S. Jang, A. N. Morozovska, O. Kwon, Y. Jin, H. Kim, H. Bae, C. Wang, H. Yang, A. Belianinov, S. Randolph, E. A. Eliseev, L. Collins, Y. Park, S. Jo, H. Jung, J. Go, H. W. Cho, Y. Choi, and Y. Kim, Science **376**, 731 (2022).

[30] A. P. C. Wylie, K. B. Woller, S. A. A. Dajani, B. R. Dacus, E. J. Pickering, M. Preuss, and M. P. Short, J. Appl. Phys. **132**, 045102 (2022).

[31] S. E. Ferry, C. A. Dennett, K. B. Woller, and M. P. Short, J. Nucl. Mater. **523**, 378 (2019).

[32] J. Wang, K. B. Woller, and B. Yildiz, ECS Trans. **111**, 809 (2023).

[33] B. D. Chalifoux, Y. Yao, K. B. Woller, R. K. Heilmann, and M. L. Schattenburg, Opt. Express **27**, 11182 (2019).

[34] K. B. Woller, *Characterization of the dynamic formation of nano-tendril surface morphology on tungsten while exposed to helium plasma*, Ph.D. thesis, Massachusetts Institute of Technology, Department of Nuclear Science and Engineering (2017).

[35] Y. Zhu, Z. X. Cai, R. C. Budhani, M. Suenaga, and D. O. Welch, Phys. Rev. B **48**, 6436 (1993).

[36] M. S. Yimei Zhu, Hong Zhang and D. O. Welch, Philosophical Magazine A **68**, 1079 (1993), https://doi.org/10.1080/01418619308219388.

[37] S. Chen, Z. Wang, L. Fan, Y. Chen, H. Ren, H. Ji, D. Natelson, Y. Huang, J. Jiang, and C. Zou, Phys. Rev. B **96**, 125130 (2017).

[38] T. Yajima, G. Oike, S. Yamaguchi, S. Miyoshi, T. Nishimura, and A. Toriumi, AIP Advances **8**, 115133 (2018).

[39] Z. Wang, X. Wang, E. Sharman, X. Li, L. Yang, G. Zhang, and J. Jiang, J. Phys. Chem. Lett. **11**, 1075 (2020).

[40] R. Nakayama, M. Maesato, T. Yamamoto, H. Kageyama, T. Terashima, and H. Kitagawa, Chem. Commun. **54**, 12439 (2018).

[41] N. Jiao, H.-D. Liu, L. Yang, Y.-P. Li, M. Zheng, H.-Y. Lu, and P. Zhang, EPL **138**, 46002 (2022).

[42] Z. Qing-Xun, G. Bo, W. Shu-Biao, B. Fang, G. Li, and L. Bao-Ting, Acta Physico - Chimica Sinica **25**, 183 (2009).

[43] P. Hohenberg and W. Kohn, Phys. Rev. **136**, B864 (1964).

[44] W. Kohn and L. J. Sham, Phys. Rev. **140**, A1133 (1965).

[45] P. Giannozzi, S. Baroni, N. Bonini, M. Calandra, R. Car, C. Cavazzoni, D. Ceresoli, G. L. Chiarotti, M. Cococcioni, I. Dabo, A. D. Corso, S. de Gironcoli, S. Fabris, G. Fratesi, R. Gebauer, U. Gerstmann, C. Gougoussis, A. Kokalj, M. Lazzeri, L. Martin-Samos, N. Marzari, F. Mauri, R. Mazzarello, S. Paolini, A. Pasquarello, L. Paulatto, C. Sbraccia, S. Scandolo, G. Sclauzero, A. P. Seitsonen, A. Smogunov, P. Umari, and R. M. Wentzcovitch, Journal of Physics: Condensed Matter **21**, 395502 (2009).

[46] P. Giannozzi, O. Andreussi, T. Brumme, O. Bunau, M. B. Nardelli, M. Calandra, R. Car, C. Cavazzoni, D. Ceresoli, M. Cococcioni, N. Colonna, I. Carnimeo, A. D. Corso, S. de Gironcoli, P. Delugas, R. A. DiStasio, A. Ferretti,

A. Floris, G. Fratesi, G. Fugallo, R. Gebauer, U. Gerstmann, F. Giustino, T. Gorni, J. Jia, M. Kawamura, H.-Y. Ko, A. Kokalj, E. Küçükbenli, M. Lazzeri, M. Marsili, N. Marzari, F. Mauri, N. L. Nguyen, H.-V. Nguyen, A. O. de-la Roza, L. Paulatto, S. Poncé, D. Rocca, R. Sabatini, B. Santra, M. Schlipf, A. P. Seitsonen, A. Smogunov, I. Timrov, T. Thonhauser, P. Umari, N. Vast, X. Wu, and S. Baroni, Journal of Physics: Condensed Matter **29**, 465901 (2017).

[47] G. Kresse and J. Furthmüller, Comput. Mater. Sci. **6**, 15 (1996).

[48] G. Kresse and J. Furthmüller, Phys. Rev. B **54**, 11169 (1996).

[49] H. Jonsson, G. MILLS, and K. JACOBSEN, Nudged elastic band method for finding minimum energy paths of transitions (World Scientific, 1998) pp. 385–404.

[50] J. F. Ziegler, SRIM.EXE (1984).